Investigation of Air-Water Flow in a Horizontal Pipe with 90 Degree Bends using Wire Mesh Sensors

Robert C. Bowden and Sun-Kyu Yang[1]
Canadian Nuclear Laboratories, Chalk River, Ontario, Canada
(robert.bowden@cnl.ca, sun-kyu.yang@cnl.ca[1])

Abstract

Wire mesh sensors were used to investigate the void fraction distribution along a 9 meter long, 50.8 mm diameter, horizontal test section that contained two 90 degree bends. Deionised water and compressed air were used as the working fluids, with the bubbly flow regime achieved at a superficial liquid velocity of 3.5 m/s and superficial gas velocities that varied between 0.1 and 1.2 m/s. The effects of superficial gas velocity and axial location on the void fraction distribution were investigated. Bubble and slug flow patterns were identified using a probability density function analysis based on a Gaussian mixture model.

1 Introduction

Two-phase gas-liquid flow has important practical applications related to the nuclear industry, and studies related to two-phase flow regimes [1], pressure drop [2], and phase distribution [3] within a variety of geometries will be of continued interest for the foreseeable future [4]. Of particular interest to typical CANDU®[2] type nuclear reactors is flow through horizontally oriented geometries due to their prevalence in the primary heat transport system which includes, for example, the pressure tubes, the calandria vessel, and the header-feeder piping network. Detailed experimental measurements are important for the development of closure relations, such as the bend dissipation length [7], and also in the validation of computational fluid dynamics (CFD) predictions from phase distributions [5]. Void fraction measurements have been performed using point measurement devices, such as conductivity and optical probes, within horizontal geometries including straight pipes [6] and bends [7]. Advancements in measurement technologies, such as wire mesh sensors (WMS) [8], have permitted whole field measurements of the local void fraction. Recently, WMS has been applied to horizontal pipes containing a single 90 degree bend [9] within stratified and annular flow regimes. However, experimental investigations near the bubbly to slug regime transition region are limited.

1.1 Problem Description

Bend effects on the void distribution dissipate within the downstream region in bubbly flows [7]. Piping networks that contain two or more bends within close proximity of one another pose an intriguing problem in that the effects of the upstream bend may not be dissipated at the inlet of the downstream bend. In this study, the effects of two closely spaced horizontal 90 degree bends on the local void fraction were experimentally investigated using wire mesh sensors in the bubbly to slug transition region. To the best of the authors' knowledge, no studies have been performed in order to investigate the void distribution across multiple horizontal bends.

[1] Corresponding author
[2] CANDU® (CANada Deuterium Uranium) is a registered trademark of CANDU Energy Inc.

2 Experimental Investigations

2.1 Test Facility

2.1.1 Test Section

A schematic of the horizontal test section is presented in Figure 1. The test section is comprised of two identical commercially available 90 degree borosilicate glass elbows, designated here as Elbow 1 and Elbow 2, respectively, and three straight sections of cast clear acrylic pipe of varying axial lengths. The axial lengths of the three straight sections are Δz_1 = 5.285 m, Δz_2 = 1.190 m, and Δz_3 = 1.595 m. Each commercial elbow has an internal diameter of 50.8 mm and a radius of curvature of 76.2 mm, and is flanged on both ends. The coordinate system follows the right hand rule with the axial direction, *z-axis*, pointing downstream. The positive *x-axis* points to the left, with the positive *y-axis* pointing out of the page.

2.1.2 Flow loop

The test section was installed in the air-water flow loop at the Canadian Nuclear Laboratories (CNL) in Chalk River, Canada, as shown in Figure 2. Deionised water was the primary working fluid, which was circulated in a closed loop. A cooling coil allowed steady control of the water inlet temperature. Plant air was supplied to the test section from a central compressor. An air diffuser was installed concentrically within the pipe at the test section inlet. The downstream tip of the diffuser was chosen as the origin (x = 0, y = 0, z = 0). Air passing through the diffuser was sheared off by the cross-flow of water thereby creating a continuous two-phase inlet condition. Control valves installed on the water inlet, air inlet, and cooling coil supply line, enabled precise control of the related mass flow rates. A data acquisition and control system was used to monitor and record related loop parameters. The loop parameters included the inlet water and air mass flow rates ($\dot{m}_F, \dot{m}_G$), the inlet water and air static pressures ($P_{F,0}$, $P_{G,0}$) and temperatures ($T_{F,0}$, $T_{G,0}$), six static pressures (P_1 to P_6) and three fluid temperatures (T_1 to T_3) along the test section, and the ambient temperature (T_{atm}) and pressure (P_{atm}).

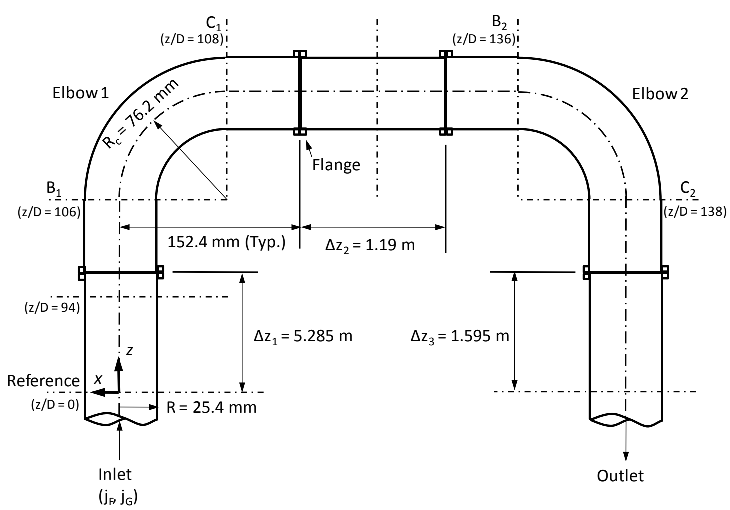

Figure 1 Schematic of the horizontal test section (top view).

2.1.3 Data Reduction: Loop Parameters

The superficial gas velocity, j_G, was defined using the gas mass flow rate, $\dot{m}_G$, gas density, ρ_G, pipe diameter, D, as,

$$j_G = \frac{4\dot{m}_G}{\pi D^2 \rho_G}, \tag{1}$$

and the superficial liquid velocity was defined using the liquid mass flow rate, $\dot{m}_F$, and liquid density, ρ_F, as,

$$j_F = \frac{4\dot{m}_F}{\pi D^2 \rho_F}. \tag{2}$$

The National Institute of Standards and Technology (NIST) properties database REFPROP [10] was used to determine fluid properties. To account for the effect of pressure and temperature on local properties, the gas phase density was defined by the ideal gas law using the absolute pressure and temperatures. Standard atmospheric pressure and temperature were taken as 101.325 kPa and 20°C.

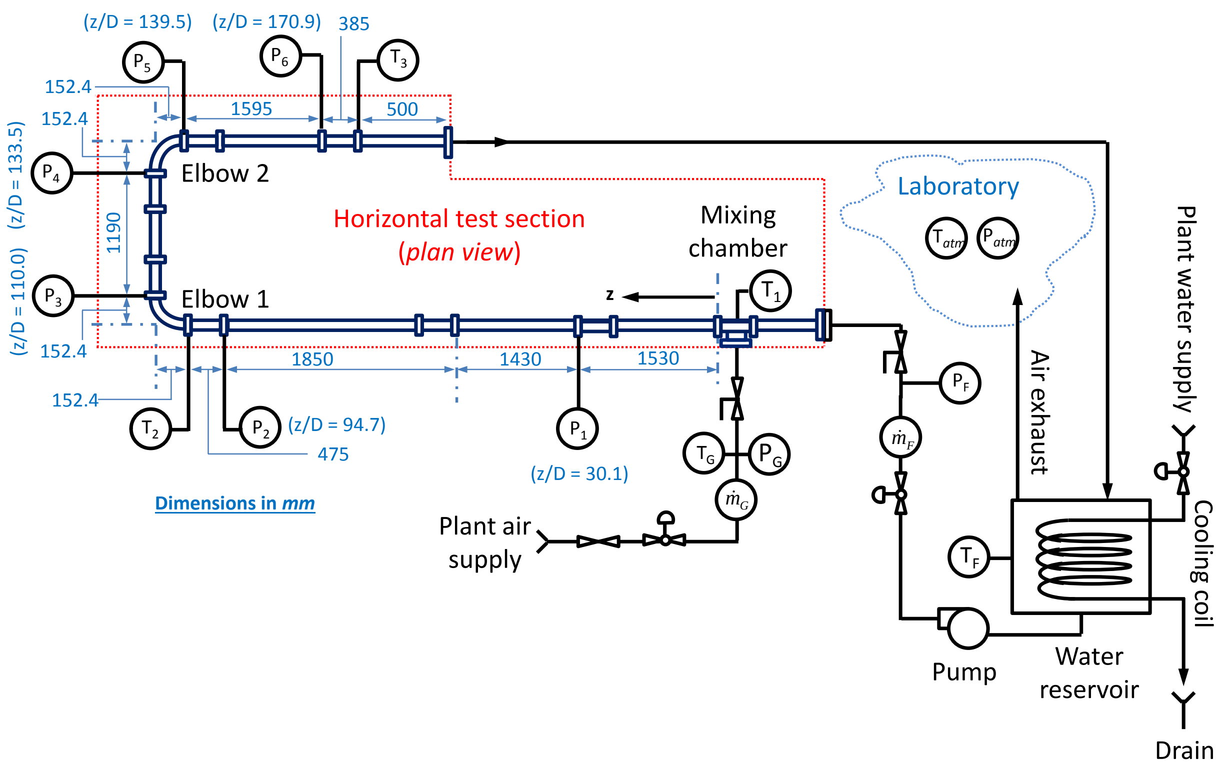

Figure 2 Schematic of the test facility.

2.2 Wire Mesh Sensor

A wire mesh sensor (WMS) system from Teletronic Rossendorf GmbH was used to perform void fraction measurements at discrete axial locations along the test section. The wire mesh sensor consists of a transmitting and receiving set of 0.125 mm diameter stainless steel wires. The transmitter wires were parallel to each other in a vertical plane and were separated by 2.117 mm. Similarly, the receiver wires were parallel to each other in the horizontal plane and offset by 2.117 mm. Void measurements were conducted at the crossing nodes of the transmitter and receiver wires. A schematic of the WMS grid is presented in Figure 3.

Using a multiplex circuit and sequential control, as described by Prasser et al. [8], the electrical conductivity of the fluid residing between the transmitter and receiver wires at each crossing node was measured. The resulting two-dimensional matrix of electrical conductivities was used to determine the local void fraction. Local void fractions at each time interval were obtained by comparing the resulting two-phase flow conductivity matrix to a single-phase liquid calibration matrix. The result was a three-dimensional matrix of local instantaneous void fractions ($\alpha_{i,j,k}$), where i, j, and k were indices for the node coordinates in x, y directions and time, t, respectively.

2.2.1 Calibration

Calibration was performed with single phase liquid flowing through the test section prior to two-phase measurements. At a given axial measurement location, the fluid conductivity matrix, U_w (x, y, t), was obtained at 5000 frames per second over a time interval of 10 seconds, and the resulting matrices were temporally averaged prior to post-processing two-phase data.

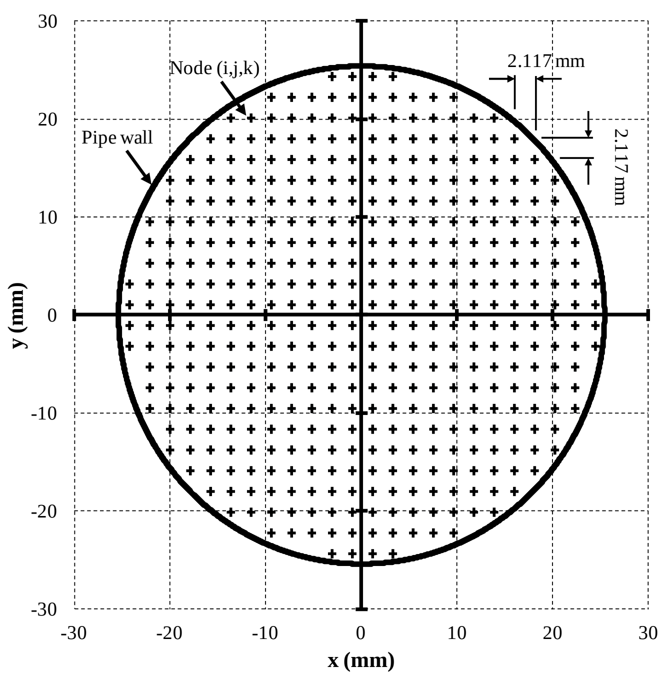

Figure 3 Schematic of the wire mesh sensor grid.

2.2.2 Data Reduction: Void Fraction

The measured two-phase flow conductivity matrices, U_{meas} (x, y, t), were compared with the temporally averaged single phase flow calibration matrix to produce instantaneous void fraction matrices. The local instantaneous void fraction was then determined by,

$$\alpha(x,y,t) = \frac{U_W - U_{meas}}{U_W}. \quad (3)$$

The void fraction matrices were averaged over the cross-sectional area using a weight coefficient matrix, $a_{i,j}$, which defined the relative weight of the differential area surrounding each crossing node. Central areas were square ($a_{i,j}$ = 1), whose side lengths were equal to the wire spacing, while edge regions were trapezoidal ($a_{i,j}$ < 1) due to the intersection of the pipe wall. The instantaneous cross-sectionally averaged void fractions were defined as,

$$\langle\alpha\rangle(t) = \sum_i \sum_j a_{i,j}\, \alpha_{i,j,k}. \quad (4)$$

Local temporally averaged void fraction distributions were determined from,

$$\bar{\alpha}(x,y) = \frac{1}{k_{max}} \sum_{k=1}^{k_{max}} \alpha_{i,j,k}, \quad (5)$$

where k_{max} was the maximum time interval index.

2.3 Test Matrix

Tests were performed under both single phase and two-phase flow conditions. The single phase flow condition runs were performed at the same superficial liquid velocity, 3.5 m/s, prior to each two-phase flow condition run for WMS calibration purposes. The objectives of the two-phase experiments were to investigate the local void fraction distributions at discrete axial locations along the test section. Table 1 presents the ranges of superficial liquid and gas velocities that were tested, along with the axial locations of the WMS sensor. It was designed to investigate both the effect of superficial gas velocity and axial location on void fraction distribution. The gas phase superficial velocities quoted in Table 1 are presented at standard atmospheric pressure at temperature, which is indicated by the subscript *atm*. Test cases are labeled using a two numbered system. The first number refers to the flow condition, while the second number refers to the axial location. For example, Case 1 refers to j_F = 3.5 m/s and $j_{G,atm}$ = 0.1 m/s, while Case 1-1 refers to the same flow condition at a specific axial location of z/D = 97.5. Experiments were performed with a steady mean water temperature of 20°C at an average measured ambient pressure and temperature of 100 kPa and 23°C, respectively. The loop parameters were recorded at 1 sample per second, and typically over a period of 100 seconds. The temporal mean of each parameter was used to define the flow condition. Two-phase WMS measurements were performed at a sampling frequency of 5 kHz for a total duration of 60 seconds.

2.4 Estimates of Experimental Uncertainty

The root-sum-squared (RSS) method for single sample measurements, outlined by Kline and McClintock [11], was used to estimate the overall experimental uncertainties at odds of 20:1. The maximum uncertainties were used to estimate the ranges quoted in Table 1.

3 Results and Discussion

3.1 Flow Visualization

The local superficial velocities of Case 1 to 3 are presented on Mandhane et al. [12]'s flow regime map in Figure 4. The local superficial gas velocity, $j_{G,local}$, denoted using subscript *local*, were determined using local gas densities. The map demonstrated that the expected flow regime was at the upper bound of the bubbly regime, just below the dispersed regime, and at the extreme right, defined by Case 3, the flow regime coincided with the bubbly to slug regime transition line.

Sample images of the observed two-phase flow regimes at Elbow 1, for Cases 1 to 3, are presented in Figure 5. From left to right in the Figure 5, the superficial liquid velocity was constant at 3.5 m/s while the superficial gas velocity increased from 0.1 to 1.25 m/s. Reference lines are shown in the figure at the bend inlet and outlet, which are denoted as *B* and *C*, respectively, as well as a line coincident with the bend centerline (*y*-*z* plane). As gas phase velocity was increased the lateral spread of bubbles at the bend inlet, about the pipe centreline was apparent. In general, the gas phase entered the bend nearly symmetrically about its centreline and moved towards the inside edge (-*x* direction) near its outlet. This can be partially explained by the centrifugal force which causing the heavier liquid phase to move away from the bend centre (+*x* direction), which displaced the lighter gas phase towards the inside. For all three flow conditions bubbles tended to accumulate towards the top of the pipe (+*y* direction) before entering the bend. Due to the circular wall, and the motion induced by the heavier liquid phase in the bend, the bubbles not only move towards the inside of the bend (-*x* direction) but towards the bottom of the pipe (-*y* direction). Near the bend outlet bubbles were tightly packed, and in this region it was expected that coalescence and break-up mechanisms would alter the bubbly flow structure.

Table 1 Test matrix for two-phase experiments.

Test case	j_F (m/s)	$j_{G,atm}$ (m/s)	WMS location (z/D)
1-1	3.5±0.20	0.10±0.02	97.5±1.2
1-2			112.8±1.4
1-3			130.8±1.6
1-4			142.3±1.7
1-5			173.6±2.1
2-1		0.42±0.08	97.5±1.2
2-2			112.8±1.4
2-3			130.8±1.6
2-4			142.3±1.7
2-5			173.6±2.1
3-1		1.25±0.24	97.5±1.2
3-2			112.8±1.4
3-3			130.8±1.6
3-4			142.3±1.7
3-5			173.6±2.1

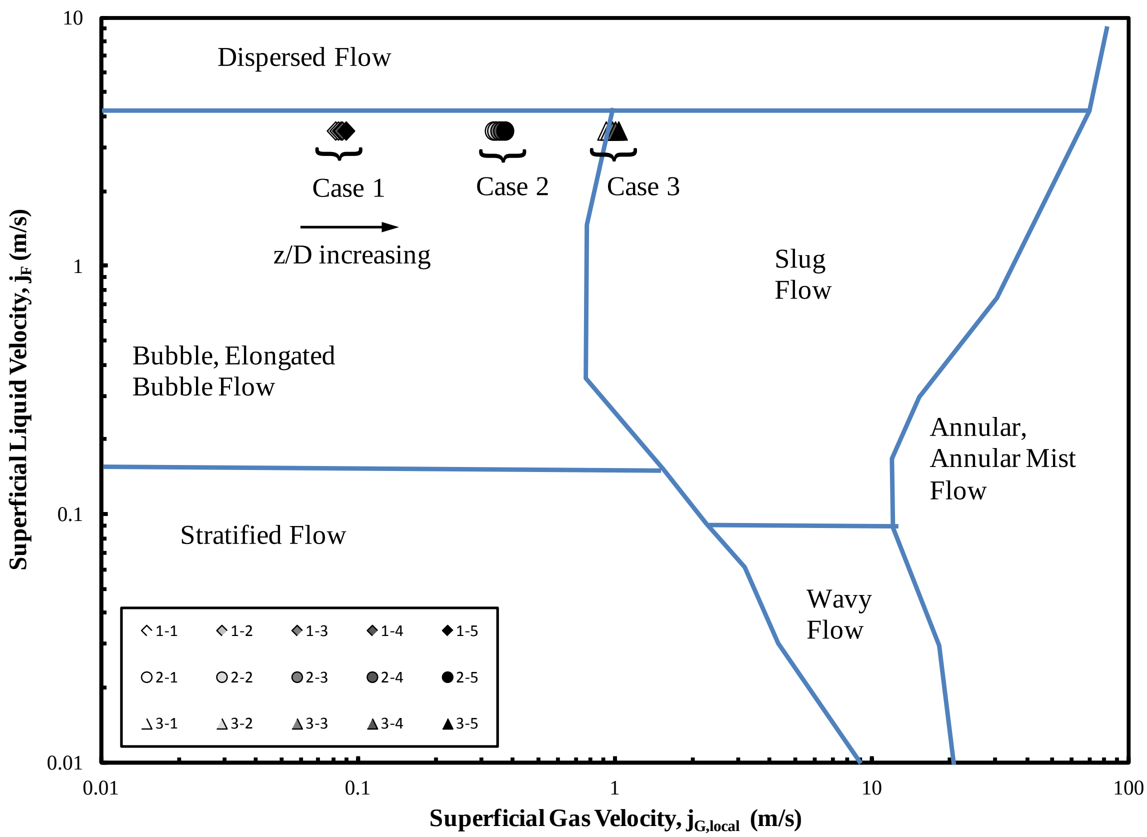

Figure 4 Local superficial velocities for Cases 1 to 3 compared to Mandhane et al. [12]'s flow regime map.

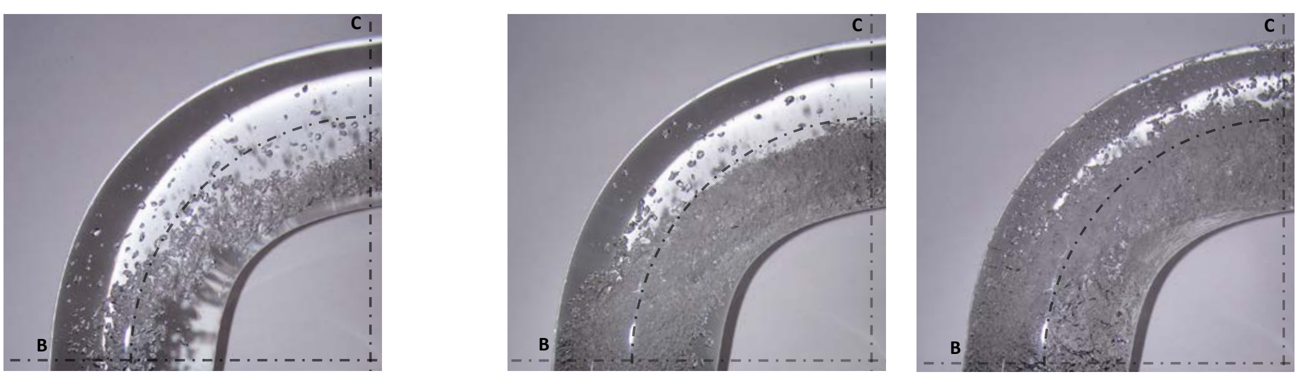

(a) (b) (c)

Figure 5 Sample images at Elbow 1 (top view) for Cases (a) 1, (b) 2, and (c) 3.

3.2 Void Fraction

A short 0.2 second sampling of the cross-sectionally averaged void fraction is presented in Figure 6. The axial location is constant in Figure 6 (a) and the superficial gas velocity is varied, while in Figure 6 (b) the superficial gas velocity is constant and the axial location is varied. Figure 6 (a) demonstrates that the cross-sectionally averaged void fraction increases with increasing superficial gas velocity, as might be expected, and there is also a noticeable increase in fluctuations with increasing superficial gas velocity. Case 1-1 exhibits the lowest fluctuation in comparison to Cases 2-1 and 3-1, with the latter cases exhibiting short bursts of high void fraction values superimposed on lower, less fluctuating, void fraction values. The frequency of the high void fraction bursts seem to increase with the superficial gas velocity. The high void fraction bursts are indicative of highly compacted bubble flow patterns, sometimes referred to as froth, which are typical of the slug regime. The flow pattern found in Case 3 is consistent with the flow regime map presented in Figure 4. The slug pattern found in Case 2, however, occurred at a much lower superficial gas velocity than expected by the flow regime map's bubbly to slug transition line. Figure 6 (b) demonstrates how the cross-sectionally averaged void fraction varies with axial location for the flow conditions of Case 2. The effects of decreasing static pressure and rotational effects due to fluid motion through the bend contribute to the variations observed between Case 2-1 and 2-5. At most axial locations, over the short time interval presented, the slug bursts continue to be present.

Statistical techniques were used to analyze each case's entire 60 second time series. Sample histograms of the 60 second time series of the cases from Figure 6 are presented in Figure 7. Figure 7 (a) demonstrates the effect of superficial gas velocity while Figure 7 (b) presents the effect of axial location. In Figure 7 (a), as the superficial gas velocity increases from Case 1-1 to 3-1 the histogram transitions from unimodal to bimodal. For Case 1-1, the nearly symmetric unimodal histogram denotes the bubbly flow pattern, while in the bimodal histogram shown in Case 3-1 the peak with the higher magnitude is associated with the bubbly regime while the second, lower magnitude peak, is associated with the high void fraction slugs. In between, Case 2-1, the unimodal histogram is not fully symmetric, which is indicative of the presence of the superimposed slug flow pattern. Figure 7 (b) demonstrates that although the mean void fraction varies somewhat, the general shape of the histogram does not vary significantly along the axial direction.

A Gaussian mixture model (GMM) analysis is presented in Figure 8 of the histograms presented in Figure 7. The GMM analysis was performed using Matlab's built-in function, *em_1dim*, which discretizes a continuous histogram into one or more probability density functions (PDF). Since at most two flow patterns were expected from flow visualization, the bubbly and slug flow patterns, the function was used to analyze the histograms into two normally distributed PDFs. In Figure 8 the black coloured lines are associated with the bubbly flow pattern, while the blue coloured lines are associated with the slug flow pattern. Figure 8 (a) demonstrates that the superimposed slug flow pattern, which is found in all cases and most weakly in Case 1-1, becomes more pronounced as the superficial gas velocity increases. The analysis also demonstrates in Figure 8 (b) that the axial location only has a small to moderate effect on the PDF distribution, the most pronounced of which occurs after the first bend, from Case 2-1 to Case 2-3. This trend was consistent in all tested cases.

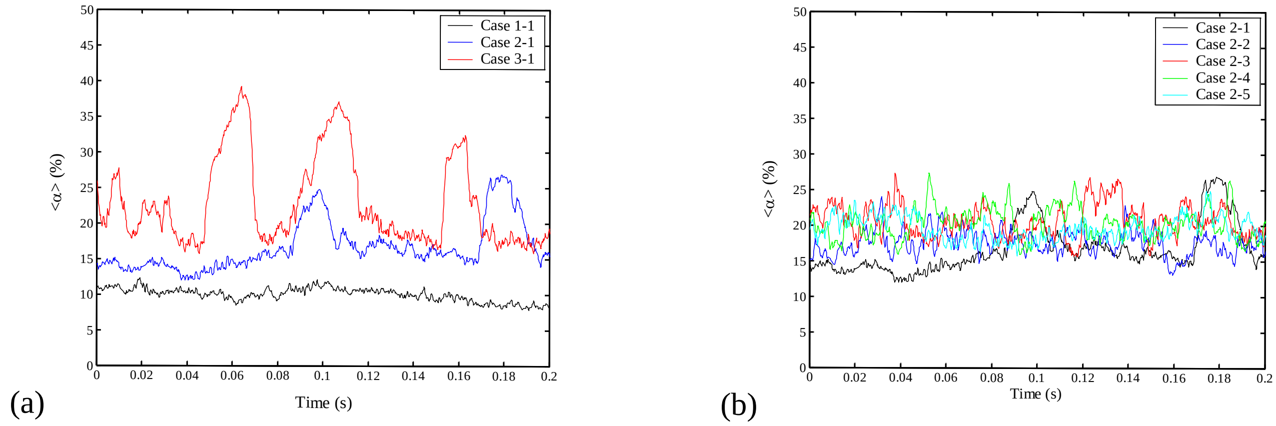

Figure 6 Sample of cross-sectionally averaged void fraction results showing the effect of (a) superficial gas velocity and (b) axial location.

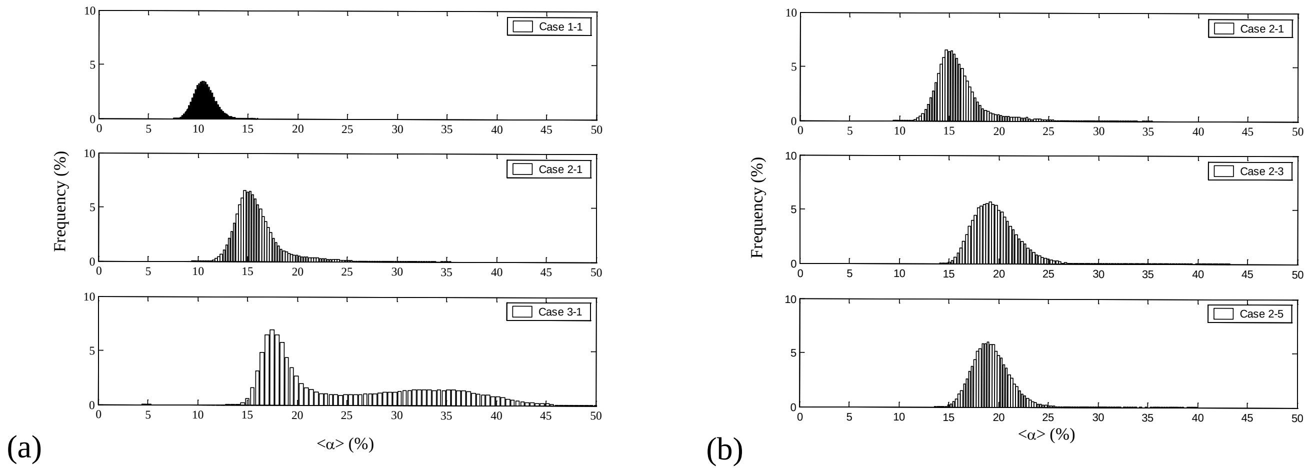

Figure 7 Histograms of cross-sectionally averaged void fraction demonstrating the effects of (a) superficial gas velocity and (b) axial location.

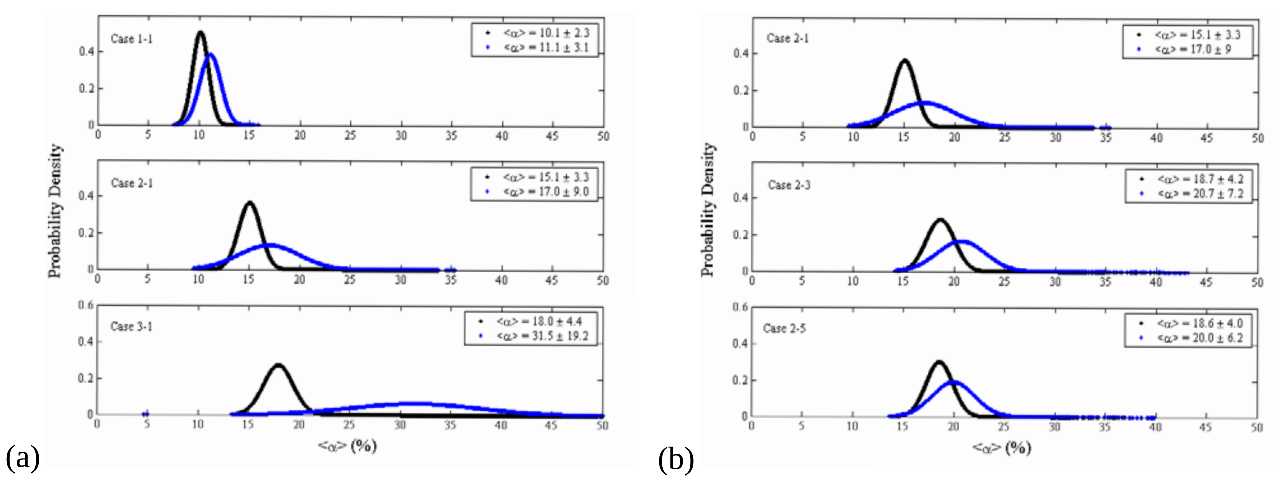

Figure 8 Normal probability density of cross-sectionally averaged void fraction demonstrating the effects of (a) superficial gas velocity and (b) axial location.

The time averaged void fraction distributions are presented as contours in Figure 9 for all test cases. The fifteen sub-figures are arranged such that rows represent constant axial locations while columns represent constant superficial gas velocities at standard atmospheric pressure. The top most row coincides with the axial location just upstream of Elbow 1, and demonstrates that the gas phase tends to accumulate towards the top half of the pipe and become more laterally distributed as superficial gas velocity increases. Immediately following Elbow 1, along the second row, the gas phase distribution is shifted to the left (-*x* direction) and downward (-*y* direction), which is consistent with the qualitative flow visualization. Along the third row from the top, which is the measurement location just upstream of the second bend, the gas phase begins to re-develop towards the top half of the pipe due to the effect of the buoyancy force. The fourth and fifth rows, which present axial locations downstream of Elbow 2, show similar effects of the second bend on the gas phase distribution shifting and re-development. In all cases, after the first bend the length of straight pipe is not sufficient long in order for the gas phase to fully re-develop to the pre-bend condition. Moreover, based on the PDF analysis, the resulting time averaged void fraction distribution along the third column is a superposition of bubbly and slug flow pattern distributions. Therefore, time averaging of the entire time interval does not reveal how the two bends affect individual flow patterns. Evaluating the area averaged void fraction over time intervals identified by specific flow patterns, such as found from GMM PDF analysis, can lead to more accurate physical descriptions of bend effects within transitional regimes.

4 Conclusions

Air water experiments were performed in a horizontal test section containing two 90 degree bends using wire mesh sensors in the bubbly flow regime, and included measurements at the bubble-slug regime transition. Flow visualization upstream of the bends confirmed that the flow regimes were consistent with established flow pattern maps. Wire mesh sensor measurements, along with probability density function analysis, confirmed however, that a second slug type flow pattern was present in the mainly bubbly regime at much lower superficial gas velocities than expected from flow regime maps. The slug regime appeared in the area averaged void fraction as bursts of high void fraction values over short time intervals. These high void fraction bursts caused asymmetry in the unimodal area averaged void fraction histogram at low superficial gas velocities. At the highest tested superficial gas velocities the area averaged histogram was found to be bimodal, which was due to the presence of both bubble and slug flow patterns. The bend effects were two-fold, with the first attributed to the pressure loss effect which caused gas phase expansion and an increase in the area averaged void fraction. The second was due to the centrifugal force causing the liquid phase to move towards the outside of the bend, which displaced the lighter phase towards the inside of the bend. The time averaged void fraction distributions were used to highlight the bend effects.

4.1 Future Directions

This study is currently being repeated using fibre optic probe technology developed at CNL in order to validate the void fraction distribution results through cross-comparison.

5 Acknowledgements

The authors recognize and appreciate the considerable efforts provided by all the technical staff within the Thermalhydraulics Branch involved in constructing and operating the experimental facility.

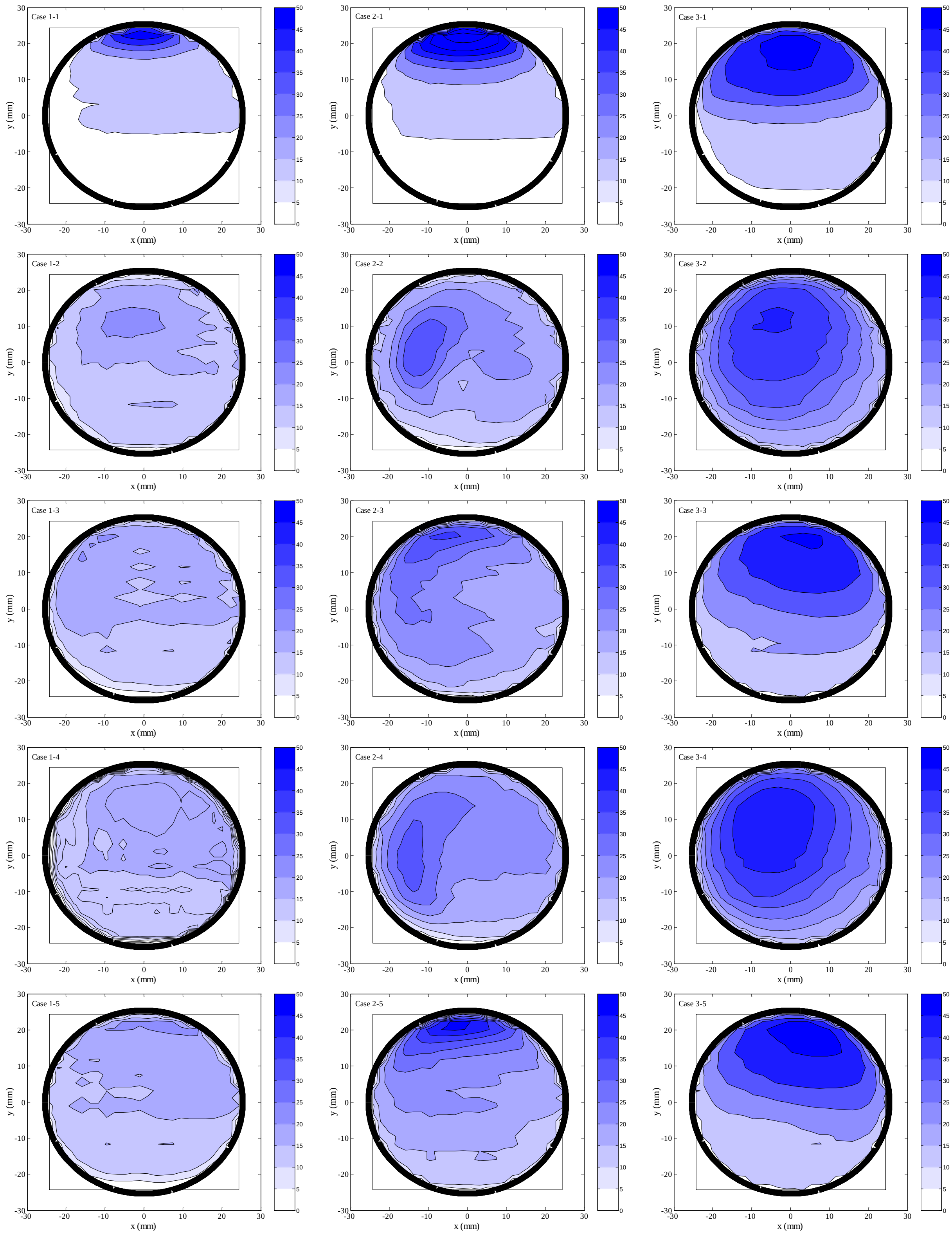

Figure 9 Contours of time averaged void fraction ($\overline{\alpha}$) for Cases 1 to 3.

6 References

[1] A. Aly, “Flow regime boundaries for an interior subchannel of a horizontal 37-element bundle” The Canadian Journal of Chemical Engineering, Vol. 59, 1981, pp.158-163.

[2] S. Supa-Amornkul, F. Steward and D. Lister, “Modeling two-phase flow in pipe bends” ASME, Journal of Pressure Vessel Technology, Vol. 127, 2005, pp.204-209.

[3] X. Yang, J. Schlegel, Y. Liu, S. Paranjape, T. Hibiki and M. Ishii, “Experimental study of interfacial area transport in air-water two phase flow in a scaled 8 x 8 BWR rod bundle”, International Journal of Multiphase Flow, Vol. 50, 2013, pp.16-32.

[4] P. Saha, N. Aksan, J. Andersen, J. Yan, J. Simoneau, L. Leung, F. Bertrand, K. Aoto, and H. Kamide, “Issues and future directions of thermal-hydraulics research and development in nuclear power reactors”, Nuclear Engineering and Design, Vol. 264, 2013, pp.3-23.

[5] G. Yeoh, S. Cheung, and J. Tu, “On the prediction of the phase distribution of bubbly flow in a horizontal pipe”, Chemical Engineering Research and Design, Vol. 90, 2012, pp.40-51.

[6] M. Bottin, J. Berlandis, E. Hervieu, M. Lance, M. Marchand, O. Ozturk, and G. Serre, “Experimental investigation of a developing two-phase bubbly flow in horizontal pipe” International Journal of Multiphase Flow, Vol. 60, 2014, pp.161-179.

[7] M. Yadav, T. Worosz, S. Kim, K. Tien, and S. Bajorek, “Characterization of the dissipation of elbow effects in bubbly two-phase flows”, International Journal of Multiphase Flow, Vol. 66, 2014, pp.101-109.

[8] H. Prasser, A. Bottger, and J. Zschau, “A new electrode-mesh tomograph for gas-liquid flows”, Flow Measurement and Instrumentation”, Vol. 9, 1998, pp.111-119.

[9] R. Vieira, N. Kesana, B. McLaury, S. Shirazi, C. Torres, E. Schleicher, and U. Hampel, “Experimental investigation of the effect of 90 standard elbow on horizontal gas-liquid stratified and annular flow characteristics using dual wire-mesh sensors”, Experimental Thermal and Fluid Science, Vol. 59, 2014, pp.72-87.

[10] E. Lemmon, M. Huber, and M. McLinden, “NIST Standard Reference Database 23: Reference Fluid Thermodynamic and Transport Properties – REFPROP Version 9.1”, National Institute of Standards and Technology, Standard Reference Data Program, Gaithersburg, MD, USA, 2013.

[11] Kline, S., & McClintock, F. “Describing uncertainties in single sample experiments” Mechanical Engineering, Vol. 75, 1953, pp. 3-8.

[12] J. Mandhane, G. Gregory, and K. Aziz, “A flow pattern map for gas-liquid flow in horizontal pipes”, International Journal of Multiphase Flow, Vol. 1, 1974, pp.537-553.